The Astrophysical Journal, 949:31 (10pp), 2023 May 20 https://doi.org/10.3847/1538-4357/acc458

Very Metal-poor Stars in the Solar Vicinity: Kinematics and Abundance Analysis

Anastasiia Plotnikova[1], Giovanni Carraro[1], Sandro Villanova[2], and Sergio Ortolani[1]
[1] Dipartimento di Fisica e Astronomia, Università di Padova, I-35122, Padova, Italy; giovanni.carraro@aas.org
[2] Departamento de Astronomia, Casilla 160-C, Universidad de Concepción, Concepción, Chile
Received 2023 January 25; revised 2023 March 13; accepted 2023 March 14; published 2023 May 24

Abstract

Very metal-poor stars contain crucial information on the Milky Way's infancy. In our previous study we derived a mean age of ∼13.7 Gyr for a sample of these stars in the Sun's vicinity. In this work, we investigate the chemical and kinematic properties of these stars with the goal of obtaining some insights into their origin and their parent population. We did not find any Al–Mg anticorrelation, which leads us to the conclusion that these stars did not form in globular clusters, while the detailed analysis of their orbital parameters reveals that these stars are most probably associated with the pristine bulge of the Milky Way. We then sketch a scenario for the formation of the Milky Way in which the first structure to form was the bulge through rapid collapse. The other components have grown later on, with a significant contribution of accreted structures.

Unified Astronomy Thesaurus concepts: Milky Way formation (1053); Field stars (2103); Metallicity (1031); Stellar kinematics (1608)

1. Introduction

Very metal-poor stars are some of the best candidates in which to study the formation and evolution of the universe and its Galactic components. The study of their chemistry and kinematics can help us to understand the chemical and dynamical properties of the first Population III supernovae. The origin of these stars contains important information about the formation history of the Milky Way.

Theoretical simulations of the formation of the Galaxy (Bullock & Johnston 2005) have shown that the halo bears the signatures of the Milky Way's assembly from smaller "building block" galaxies. Recent astrometric studies have shown the existence of kinematic signatures that indicate past accretion events (Belokurov et al. 2018; Myeong et al. 2019; Yuan et al. 2020). That means that the kinematics of very metal-poor stars is an important testbed for theories of the formation and evolution of the Galaxy. In fact, stars with very low metal abundances are potential members of accreted dwarf galaxies and/or clusters.

Two main theories have been suggested for the Milky Way formation. The first is the hierarchical scenario, which tells us that our Galaxy was formed through hierarchical merging of smaller dark halos. The accretion of baryonic matter occurred later. The bulge was formed first, followed by the thin disk. The thick disk could have been produced by the kinetic heating induced by small/medium-mass engulfing companions.

The presence of stellar streams in the stellar halo supports the hierarchical scenario (Helmi 2002; Ibata et al. 2002): they are tidal remains of past merger events (Grillmair 2017). Nowadays, we have a number of confirmed accretion events such as Sagittarius dwarf galaxy, Gaia–Enceladus/Sausage, Sequoia, Helmi stream, and Thamnos, while other streams were found to be associated with accreted globular clusters (Koppelman et al. 2019). The halo of the Galaxy could have mostly been assembled in a sequence of minor mergers. Furthermore, the fact that the merging frequency is increasing with redshift tells us that merging events were quite common in the infant Galaxy. That lends further support to the hierarchical scenario.

The second and most successful scenario is secular evolution (SE), with slow but continuous accretion of external matter. According to this theory, the bulge of the Galaxy was formed due to the accretion of disk matter through bar instabilities. This scenario is in agreement with the observed color gradient and the relation between the color of the bulge and disk studied through statistical analysis of 257 spiral galaxies (Gadotti & dos Anjos 2001). SE is also supported by the relation between the bulge and disk masses and radii (Courteau et al. 1996).

Metal-poor stars, being mostly ancient, are ideal probes of the early evolutionary phases of the universe. Because of their low metallicity, they are linked to the most pristine star formation episodes in the universe.

In this work, we build on Plotnikova et al. (2022) and study the kinematics and abundances of a sample of very metal-poor stars in the solar vicinity. Therefore, the layout of this study is as follows. In Section 2 we discuss the data upon which our study is based. Sections 3 and 4 are focused on the chemistry and kinematics of our stars, respectively. The results of our investigation are detailed in Section 5, while Section 6, finally, summarizes the outcome of this study and highlights future perspectives.

2. Data

As the main target for this investigation, we chose the data set of 28 very metal-poor stars for which we derived precise ages (Plotnikova et al. 2022). These stars are of particular interest because they are very metal-poor and their average age is 13.7 ± 0.4 Gyr. As a result, the stars in this sample are valuable candidates for studying the early stages of the formation of the Galaxy.

2.1. Distance Determination

Distance is one of the most important parameters in dynamics studies. In Plotnikova et al. (2022) we compared the best distances, estimated by four different techniques: Gaia

Table 1
Uncertainties of Astrometry from Gaia Early Data Release 3 (Gaia Collaboration 2021)

Data Product or Source Type	Typical Uncertainty			
	$G < 15$	$G = 17$	$G = 20$	$G = 21$
Five-parameter astrometry				
Position (mas)	0.01–0.02	0.05	0.4	1
Parallax (mas)	0.02–0.03	0.07	0.5	1.3
Proper motion (mas yr^{-1})	0.02–0.03	0.07	0.5	1.4
Six-parameter astrometry				
Position (mas)	0.02–0.03	0.08	0.4	1
Parallax (mas)	0.02–0.04	0.1	0.5	1.4
Proper motion (mas yr^{-1})	0.02–0.04	0.1	0.6	1.5

Note. G is the G-band Gaia Early Data Release 3 photometry.

EDR3 parallaxes (Gaia Collaboration 2021), Gaia EDR3 (Gaia Collaboration 2021) corrected by Lindegren et al. (2021), the distances derived by Bailer-Jones et al. (2021), and Queiroz et al. (2020, `StarHorse`). Our choice was made based on the best fit of the data with the isochrones in the color–magnitude diagram. As a result, we found that the best distances are those obtained directly from Gaia DR3 parallaxes (Plotnikova et al. 2022).

2.2. Astrometric Parameters

With the goal of calculating orbits and orbital parameters, we extracted coordinates, radial velocities, and proper motion components from the Gaia DR3 archive (Gaia Collaboration et al. 2022). Uncertainties for astrometric parameters are shown in Table 1. Position and velocity of the stars in equatorial coordinates were transformed to Galactocentric coordinates by the Python package `astropy` (Astropy Collaboration et al. 2013, 2018, 2022).[3]

3. Chemistry

All our stars are from the Hamburg versus ESO R-process Enhanced Star (HERES) survey. The chemical abundances were spectroscopically studied by Barklem et al. (2005). The spectrum synthesis assumes LTE and a 1D plane-parallel model of the atmosphere, where turbulence is modeled through the classical microturbulence and macroturbulence parameters. Their "snapshot" spectra cover a wavelength range of 3760–4980 Å and have an average signal-to-noise ratio of S/N $\sim$ 54 per pixel over the entire spectral range. A 2″ slit is employed giving a minimum resolving power of $R \approx 20{,}000$. From the "snapshot" spectra the elemental abundances of moderate precision (absolute rms errors of order 0.25 dex, relative rms errors of order 0.15 dex) have been obtained for 22 elements: C, Mg, Al, Ca, Sc, Ti, V, Cr, Mn, Fe, Co, Ni, Zn, Sr, Y, Zr, Ba, La, Ce, Nd, Sm, and Eu. The abundances used in this work are listed in Table 2.

3.1. Non-LTE Corrections

As mentioned above, spectral analysis in Barklem et al. (2005) was done assuming only the LTE model. However, aluminum abundance was obtained from the lines in the ultraviolet part of the spectrum that are significantly affected by non-LTE effects (Nordlander & Lind 2017). To improve the precision of the chemical parameters we applied the non-LTE correction from Nordlander & Lind (2017). The correction was implemented for each star according to its effective temperature ($T_{\rm eff}$), metallicity ([Fe/H]), and gravity ($\log g$). The resulting corrections are on average around 0.5 dex (Table 2).

We also checked non-LTE corrections for all other elements by means of the MPIA webtool database,[4] but in all cases corrections are less than 0.1 dex and were considered negligible.

4. Kinematics

We obtained orbits and orbital parameters for all stars in the data set using parallaxes, proper motions, and radial velocities from Gaia DR3 by numerical calculation and by adopting a model of Galactic potentials. The results are then analyzed to obtain insights into the stars' origin.

4.1. Galactic Axisymmetric Potential

We corrected the velocities of the stars by the velocity of the Sun with respect to the Galactic center, which is computed independently from the velocity of the local standard of rest (Reid & Brunthaler 2004; Drimmel & Poggio 2018; GRAVITY Collaboration et al. 2018):

$$v_{R\odot} = -12.9 \pm 3.0 \text{ km s}^{-1} \quad (1)$$

$$v_{\phi\odot} = 245.6 \pm 1.4 \text{ km s}^{-1} \quad (2)$$

$$v_{Z\odot} = 7.78 \pm 0.09 \text{ km s}^{-1} \quad (3)$$

where the distance between the Galactic center and the Sun is $R_0 = 8.122 \pm 0.033$ kpc (GRAVITY Collaboration et al. 2018). We used the McMillan (2017) Galactic potential without bar implementation in `galpy`[5] (Bovy 2015) to calculate orbits and orbital parameters such as the total energy (E_n), angular momentum along the z-axis (L_z), eccentricity (e), apocenter ($R_{\rm apo}$), and pericenter ($R_{\rm peri}$).

4.2. Galactic Nonaxisymmetric Potential

To take into account the effect of the bar we replaced the axisymmetric bulge from McMillan (2017) with a nonaxisymmetric elongated bar/bulge component. As a model for the bar/bulge structure, we used the rotating ellipsoid (Chemel et al. 2018; Yeh et al. 2020) with density distribution given by Ferrer's formula (Bovy 2015):

$$\rho(x, y, z) = \begin{cases} \rho_c(1 - m^2)^2 & \text{if } m < 1, \\ 0 & \text{if } m > 1, \end{cases} \quad (4)$$

where $m^2 = x^2/a^2 + y^2/b^2 + z^2/c^2$. For the parameters, we used $a = 5$ kpc, $b = 2$ kpc, and $c = 1$ kpc, which gives a good approximation for the observed bar/bulge component in the center of the Milky Way (Portail et al. 2015, 2017). The central density of the bar is given by $\rho = (105/32\pi)GM_b/abc$, where the mass of the bar $M_b = 1.88 \times 10^{10}\, M_\odot$ (Portail et al. 2017).

The Milky Way bar is rotating around the Galactic center with constant angular velocity Ω_b. Also, its major axis is tilted

[3] https://docs.astropy.org/en/stable/_modules/astropy/coordinates/builtin_frames/galactocentric.html

[4] https://nlte.mpia.de

[5] http://github.com/jobovy/galpy

Table 2
Chemistry

ID	[Mg/Fe] (dex)	$[Al/Fe]_{LTE}$ (dex)	$[Al/Fe]_{NLTE}$ (dex)	[Ca/Fe] (dex)	[Cr/Fe] (dex)	[Ti/Fe] (dex)	[Ni/Fe] (dex)	[Fe/H] (dex)	Age (Gyr)	Origin[a]
HE_0023-4825	0.22	−1.01	−0.51	0.26	0.00	0.31	−0.01	−2.06	14.62 ± 0.11	Pr.B.
HE_0109-3711	⋯	⋯	⋯	0.42	−0.06	0.38	⋯	−1.91	11.78 ± 0.04	5G/GE
HE_0231-4016	0.22	−1.09	−0.50	0.36	−0.11	0.25	−0.14	−2.08	14.37 ± 0.47	Pr.B.
HE_0340-3430	0.19	−1.00	−0.61	0.36	−0.16	0.25	−0.26	−1.95	13.32 ± 0.13	5G/GE
HE_0430-4404	0.29	−0.97	−0.57	0.33	−0.02	0.32	0.01	−2.07	10.15 ± 1.38	Th.1
HE_0447-4858	0.24	−0.81	−0.42	0.24	0.09	0.28	0.33	−1.69	13.28 ± 0.20	5G/GE
HE_0501-5139	0.19	⋯	⋯	0.34	−0.24	0.39	−0.13	−2.38	8.93 ± 0.03	Th.1
HE_0519-5525	0.41	−0.76	−0.26	0.37	−0.19	0.37	0.13	−2.52	13.46 ± 0.06	5G/GE
HE_0534-4615	0.22	−0.87	−0.37	0.28	−0.18	0.19	−0.20	−2.01	14.91 ± 0.49	Pr.B.
HE_1052-2548	0.16	−0.48	−0.11	0.27	−0.12	0.45	0.03	−2.29	15.70 ± 0.14	Pr.B.
HE_1105+0027	0.47	−0.89	−0.33	0.47	0.05	0.32	−0.29	−2.42	12.06 ± 0.35	Th.1
HE_1225-0515	0.18	−1.00	−0.62	0.27	−0.08	0.34	−0.16	−1.96	14.64 ± 0.03	Pr.B.
HE_1330-0354	0.32	−0.93	−0.46	0.40	−0.05	0.54	−0.08	−2.29	13.49 ± 0.34	SimD
HE_2250-2132	0.31	−1.07	−0.57	0.29	−0.12	0.35	0.05	−2.22	13.19 ± 0.11	SimD
HE_2347-1254	0.29	−0.74	−0.42	0.37	−0.13	0.39	−0.16	−1.83	14.56 ± 0.03	Pr.B.
HE_2347-1448	0.13	−1.11	−0.64	0.21	−0.05	0.31	0.27	−2.31	8.63 ± 0.07	5G/GE
HE_0244-4111	0.34	⋯	⋯	0.37	−0.19	0.30	0.00	−2.56	12.75 ± 0.51	Th.1
HE_0441-4343	0.32	−1.09	−0.59	0.18	−0.36	0.27	0.07	−2.52	10.41 ± 0.50	Th.1
HE_0513-4557	0.34	⋯	⋯	0.21	⋯	⋯	⋯	−2.79	12.42 ± 0.50	OrNC
HE_0926-0508	0.28	−0.90	−0.49	0.37	−0.14	0.49	−0.06	−2.78	14.79 ± 0.51	Pr.B.
HE_1006-2218	⋯	−0.79	−0.46	0.32	−0.11	0.48	⋯	−2.69	12.90 ± 0.51	Th.2
HE_1015-0027	0.35	−1.00	−0.67	0.41	−0.24	0.55	−0.10	−2.66	15.20 ± 0.55	Pr.B.
HE_1126-1735	0.31	−1.06	−0.46	0.32	−0.29	0.33	−0.04	−2.69	9.44 ± 0.50	GE
HE_1413-1954	⋯	⋯	⋯	0.33	⋯	⋯	⋯	−3.22	14.20 ± 0.82	Pr.B.
HE_2222-4156	0.42	−0.93	−0.42	0.35	−0.21	0.33	−0.02	−2.73	13.50 ± 0.52	Th.1
HE_2325-0755	0.31	−1.02	−0.42	0.46	−0.29	0.35	−0.18	−2.85	13.50 ± 0.51	SimD

Note.
[a] GE—Gaia–Enceladus/Sausage, Th.1—Thamnos 1, Th.2—Thamnos 2, Pr.B.—primordial bulge, 5G/GE—group of five stars with a high probability of belonging to the GE, SimD—similar to the disk kinematics, OrNC—origin is not clear, stars have halo kinematics and chemistry.

with respect to the Sun. Recent measurements of the bar's angular velocity give the following results: $\Omega_b = 41 \pm 3$ km s^{-1} kpc^{-1} (Sanders et al. 2019), $\Omega_b = 37.5$ km s^{-1} kpc^{-1} (Clarke et al. 2019), and $\Omega_b = 40$ km s^{-1} kpc^{-1} (Sormani et al. 2015). In this work we used $\Omega_b = 40$ km s^{-1} kpc^{-1}, which is in good agreement with Portail et al. (2015, 2017) and Bovy et al. (2019). For the bar's orientation relative to the Sun we used $\phi = 28°$, which is in good agreement with recent estimates (Wegg & Gerhard 2013; Bland-Hawthorn & Gerhard 2016; Portail et al. 2017).

4.3. Uncertainty

To estimate uncertainties for each derived orbital parameter we perform a Monte Carlo analysis using 1000 random draws on the input parameters: parallax, radial velocity, and proper motion. We considered errors in R.A. and decl. to be negligible compared to other parameters. As for proper motion, we used the multivariate normal distribution, which takes into account the correlation between the two components.[6] For parallax and radial velocity we used just a normal distribution.

Since we use parallaxes, the resulting distribution of each orbital parameter is not Gaussian. Therefore, we derived for each orbital parameter a median value and a confidence interval of 68%.

[6] https://gea.esac.esa.int/archive/documentation/GEDR3/Gaia_archive/chap_datamodel/sec_dm_main_tables/ssec_dm_gaia_source.html

5. Results

We studied the chemical composition and kinematics of our data set of 28 metal-poor stars and the correlation with their age.

5.1. Chemistry

In Figure 1 we compared the chemical composition of our data set with bulge (red open triangles, Howes et al. 2016) and halo (gray circles, Yong et al. 2013; Roederer et al. 2014) stars of the Milky Way. Inspecting this figure, one can readily see that all our stars are in good agreement with the typical trends for Milky Way stars. This holds except for aluminum, whose position is shifted on average by 0.2 dex. For all stars we applied the non-LTE correction from Nordlander & Lind (2017), which has an important effect on the aluminum abundance.

To separate stars from the halo, the thin disk, and the thick disk we used the Al versus Mg map (Figure 2). For comparison we used: Fulbright (2000), Reddy et al. (2003, 2006), Simmerer (2004), Francois et al. (2007), and Johnson et al. (2012, 2014) for disk; Yong et al. (2013) and Roederer et al. (2014) for halo; and Howes et al. (2016) for bulge. All our stars having measurements for both elements occupy the expected region for halo stars. At odds with globular clusters' stars, our sample stars do not show any Al–Mg anticorrelation (Lucey et al. 2022; Sestito et al. 2023).

We can therefore conclude that our stars possess the typical chemical composition of field stars in the Milky Way halo. The

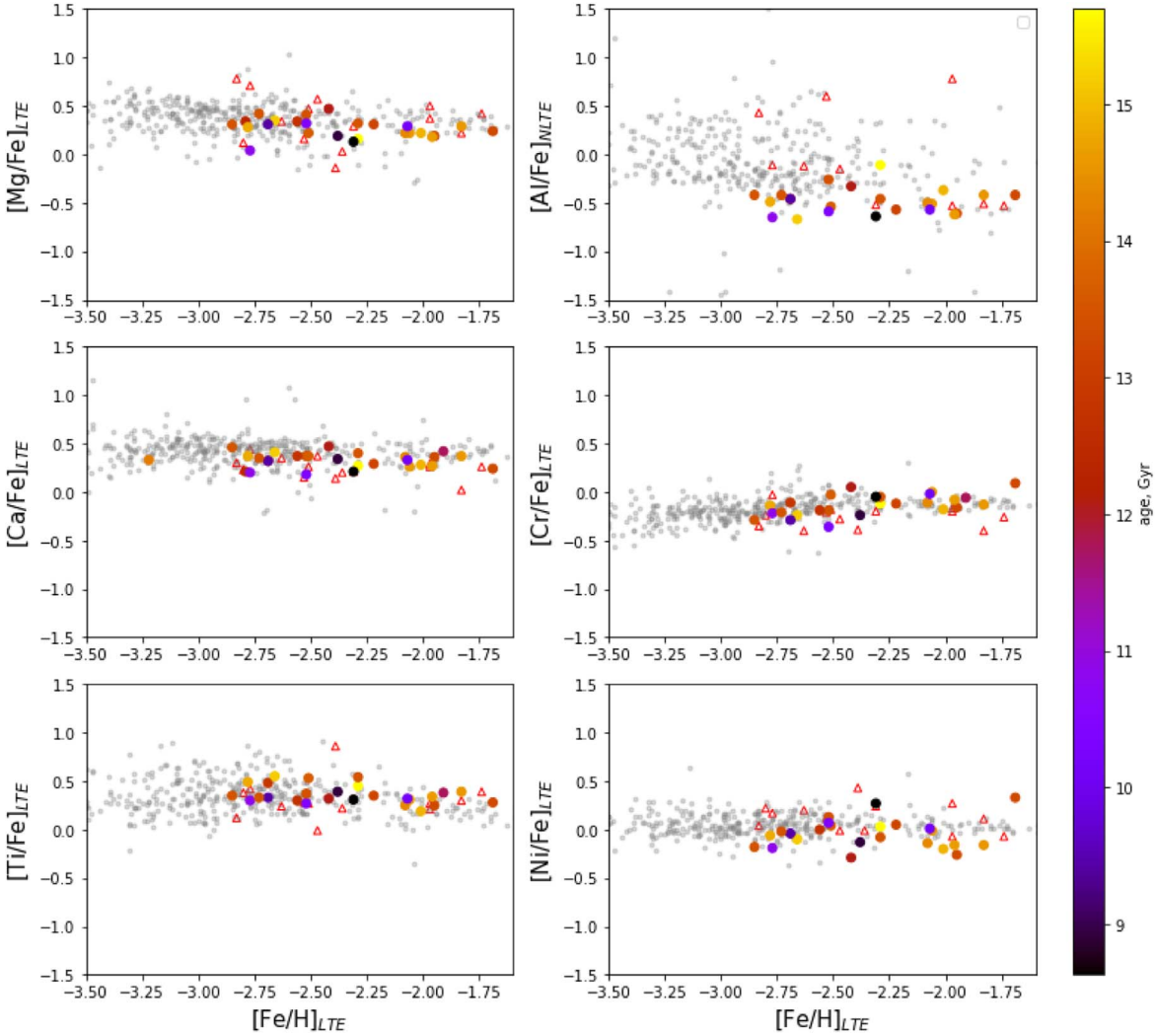

Figure 1. Correlation between iron and other chemical elements color-coded with the age. For comparison we show bulge (red open triangles, Howes et al. 2016) and halo (gray circles, Yong et al. 2013; Roederer et al. 2014) stars of the Milky Way. For all sources the Al correction from Nordlander & Lind (2017) was applied.

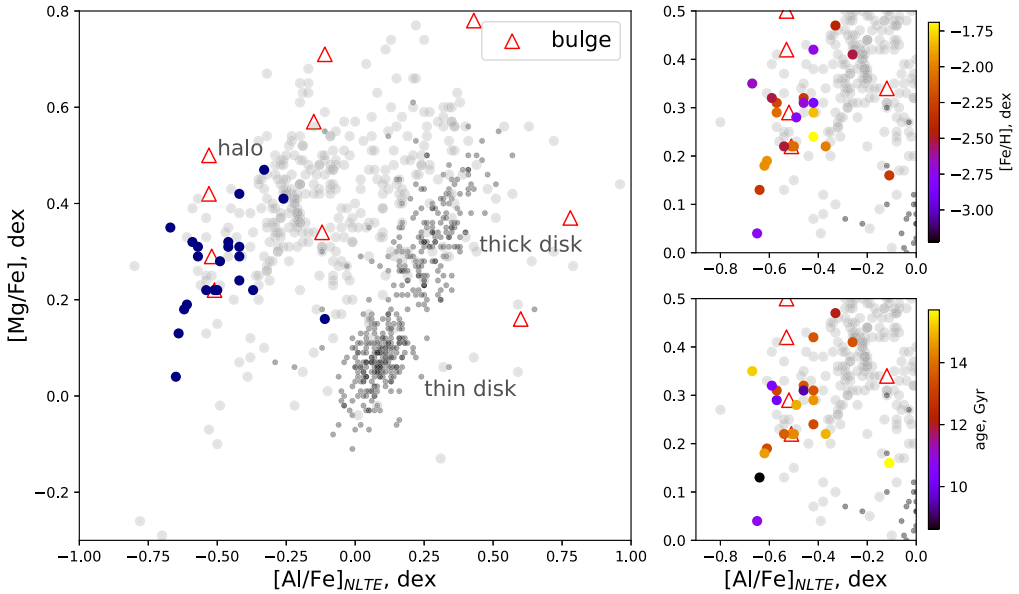

Figure 2. Al–Mg correlation. Top right: color-coded with metallicity, bottom right: color-coded with age. The background: disk stars (black dots, Fulbright 2000; Reddy et al. 2003, 2006; Simmerer 2004; Francois et al. 2007; Johnson et al. 2012, 2014), halo stars (gray points, Yong et al. 2013; Roederer et al. 2014), bulge stars (red open triangles, Howes et al. 2016).

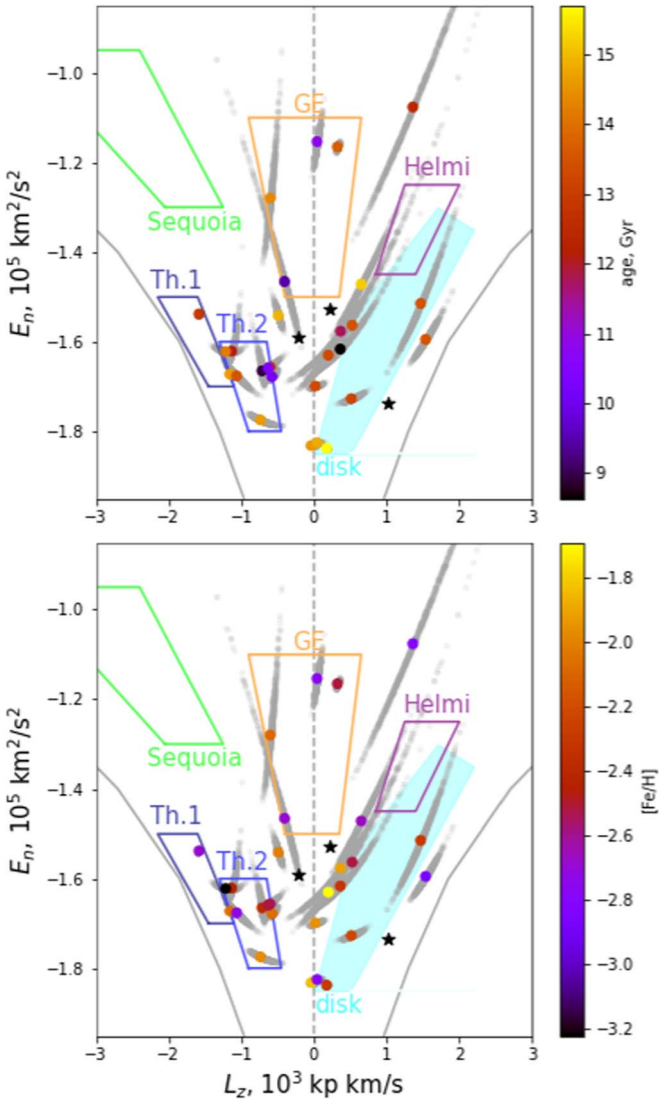

Figure 3. E_n–L_z diagram with the loci of the biggest known accretion events: Gaia–Enceladus/Sausage (GE, orange), Helmi stream (purple), Sequoia (green), Thamnos 1, 2 (dark blue, blue), and disk (cyan). Black star symbols indicate Vandenberg halo stars (VandenBerg et al. 2014). The colored points are mean values of stars under investigations, while gray trails indicate their uncertainties.

lack of any anticorrelation seems to exclude an origin inside globular clusters.

5.2. Kinematics

To get additional insight into the origin of these stars we explore their kinematic properties. To this aim, in Figure 3 we compared our results with Koppelman et al. (2019). We used the same McMillan (2017) potential as in Koppelman et al. (2019) but, after checking that there are no differences, we adopted the most recent estimates of the Sun's velocity and distance from the Galactic center (Section 4.1). Figure 3 shows that some of the stars share the same kinematics as well-known accretion events: the Gaia–Enceladus/Sausage system (orange; Belokurov et al. 2018; Helmi et al. 2018) and Thamnos 1, 2 (dark blue, blue; Koppelman et al. 2019). This result is also supported by the velocity and L_z–eccentricity diagrams (Figure 4).

Besides, we can notice a group of five stars below the Gaia–Enceladus/Sausage locus with similar orbital parameters, age, and metallicity, and a location inside the sphere with radius $R \sim 1$ kpc. In some sources, the Gaia–Enceladus/Sausage locus is extended to lower energies (Koppelman et al. 2019), which gives a higher probability for this group of five stars indeed being part of the Gaia–Enceladus/Sausage. Moreover, there are three stars (Figure 4, black dots) that exhibit disk kinematics, although their chemistry looks more similar to that of the halo.

Our stars exhibit both prograde and retrograde motion and they cover almost the entire eccentricity range (Figure 4, lower panel). Additionally, all stars are distributed around $v_\phi = 0$ km s^{-1}, which indicates a typical halo kinematics (Figure 4, upper right panel). They might be part either of Gaia–Enceladus/Sausage (GE, orange) or of Thamnos 1, 2 (dark blue, blue) accretion events. All diagrams in Figure 4 are color-coded according to their position in the L_z–E_n diagram (Figure 4, upper left panel).

However, the kinematic analysis alone is not sufficient to identify the origin of these stars and decipher whether they are associated or not with a specific accreted structure. To check the possible membership of blue and orange stars to Gaia–Enceladus/Sausage (GE, orange) or Thamnos 1, 2 (dark blue, blue) we need to combine kinematics with chemistry. In Figure 5 we can see that the Milky Way stars and accretion events possess similar chemistry.

Overall, our metal-poor stars have chemistry compatible with trends in accretion events. Additionally, we compared the age of the stars with the age of each accretion event (Figure 6), and some of the stars' ages fall into the range at the beginning of the formation of the accreting blocks. But some of the stars from this work are older and can be excluded from being accreted through known accretion events.

5.3. Orbital Parameters

In Figure 7 we present the correlation between eccentricity (e), pericenter ($R_{\rm peri}$), maximum height above the Galactic plane ($Z_{\rm max}$), and apocenter ($R_{\rm apo}$) color-coded with age. From the upper plot in Figure 7 we can notice that almost all stars in our data set cross the bulge region. That means that these stars' kinematics are perturbed by the bar/bulge potential. One can also speculate that they can be a part of the pristine bulge of the Milky Way. From the middle plot in Figure 7 we can see that the most distant stars exhibit on average more elongated orbits. The lower plot in Figure 7 shows that most of the stars have $R_{\rm apo} > Z_{\rm max}$, i.e., they lie close to the Galactic plane. Another intriguing feature in this plot is that one can readily see a clear trend in age: the oldest stars (yellow) are located nearer to the plane while the younger (redder) stars lie closer to the dashed line $R_{\rm apo} = Z_{\rm max}$.

By inspecting Figure 8 we can highlight also the following trends:

1. Eccentricity increases with increasing age.
2. The older stars orbit closer to the Galactic center and the Galactic disk.

5.3.1. Very Old Stars

Let us focus on stars with ages greater than 13.5 Gyr. Their age implies they have a very low probability of being part of

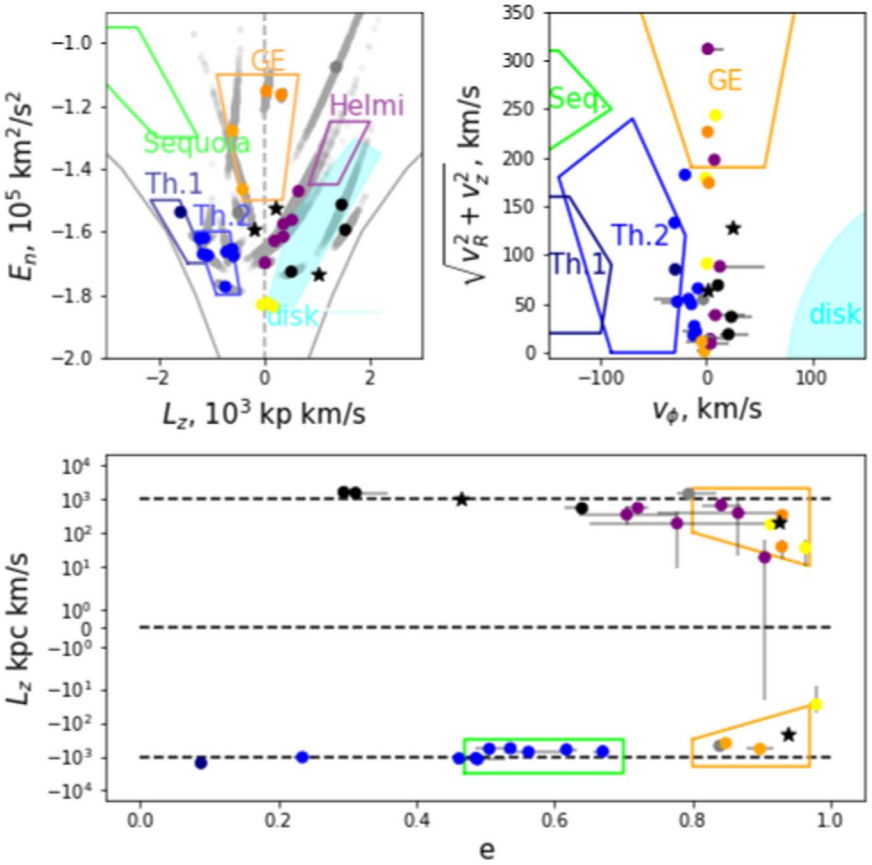

Figure 4. Points are color-coded with the position in the E_n–L_z diagram: Gaia–Enceladus/Sausage (GE, orange), Sequoia (green), Thamnos 1, 2 (Th., dark blue, blue), Sagittarius (red), disk (black), group of five stars with similar parameters (purple), low-energy stars (yellow), Vandenberg stars (VandenBerg et al. 2014, black stars).

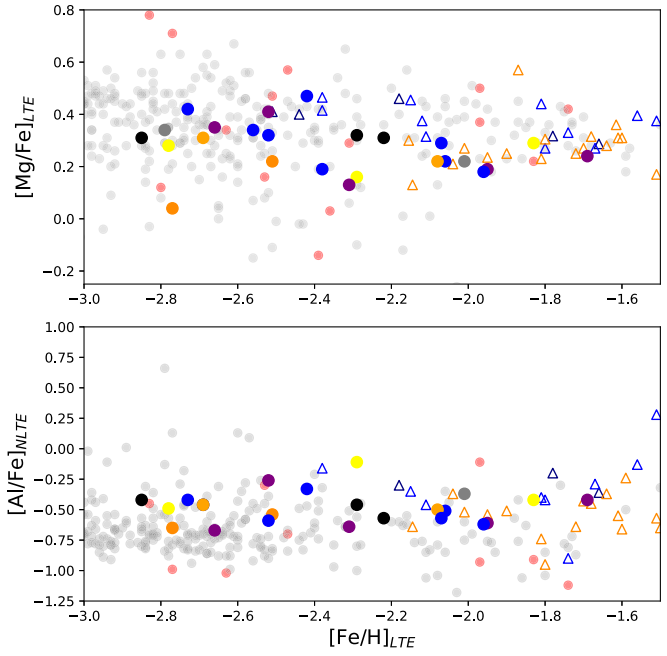

Figure 5. Correlation between Mg, Al, and Fe. For comparison, we show bulge (red circles, Howes et al. 2016) and halo (gray circles, Yong et al. 2013; Roederer et al. 2014) stars of the Milky Way. Points are color-coded with the position in the E_n–L_z diagram: Gaia–Enceladus/Sausage (orange), Sequoia (green), Thamnos 1, 2 (dark blue, blue), Sagittarius (red), disk (black), group of five stars with similar parameters (purple), and low-energy stars (yellow). Circles denote stars from this work; open triangles are stars from known accretion events (Koppelman et al. 2019).

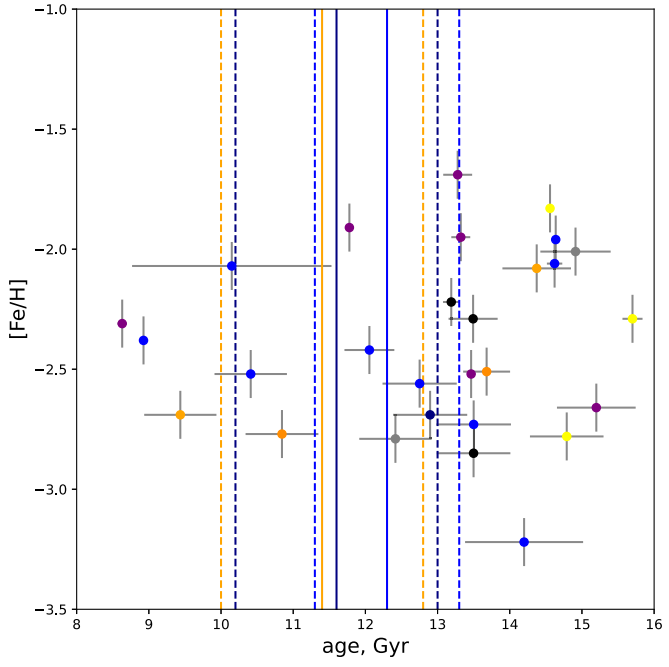

Figure 6. Age–metallicity relation with the time bars for the formation of the Gaia–Enceladus/Sausage (orange) and Thamnos 1, 2 (dark blue, blue) (Ruiz-Lara et al. 2022). Solid lines are mean values and dashed lines represent uncertainties.

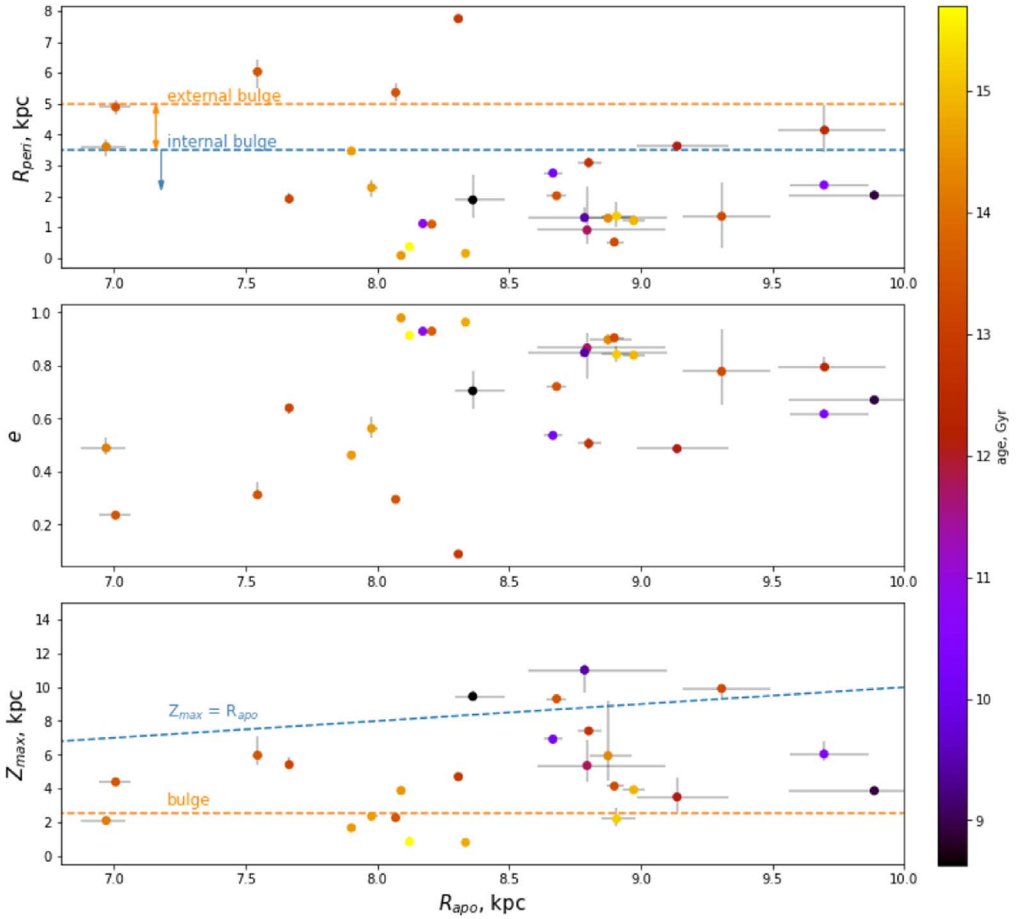

Figure 7. Correlation between eccentricity (e), pericenter ($R_{\rm peri}$), maximum height above the Galactic plane ($Z_{\rm max}$), and apocenter ($R_{\rm apo}$) color-coded with age.

any well-known accretion event (Figure 6). Additionally, their age is very close to the age of the universe and the very first instant of formation of the Milky Way. We then speculate that they can have formed inside the very first "building blocks" of the Milky Way and therefore were part of the infant bulge at a time when the disk had yet to form (Carraro et al. 1999).

Moreover, all of them have orbits close to the Galactic disk and pass close to the Galactic center while crossing the Galactic bulge. This might lend further support to a scenario in which these stars were formed in a pristine bulge and later displaced into more eccentric orbits by some migration phenomenon. The same result was obtained by Grenon (1985) for metal-rich bulge stars in the solar vicinity. However, closeness to the Galactic plane is rather the result of the observational limitations (all of our stars lie within a 5 kpc sphere around the Sun) than an intrinsic feature. We consider that with better observations there is a probability of finding old metal-poor stars passing through the bulge in elongated orbits in all directions from the Galactic center.

Returning to chemistry, stars under investigation are α-enhanced, and close to typical of today's Milky Way halo stars. According to the data of Howes et al. (2016), the chemical composition of bulge stars is more disperse than that of halo stars but distributed around the same mean, which makes it impossible to distinguish between bulge and halo stars. Still, and interestingly, for all stars in our data set there is a clear correlation between the abundance of α-elements and age (Figure 9) with weighted Pearson correlation coefficient equal to 0.24. This is due to the fact that for low-metallicity stars the main source of α-elements is supernovae of Type II (SNe II). An increasing α-abundance can be a signature of an environment where gas density and star formation were quite high. This seems to be another argument in favor of the idea that our oldest stars were associated with the ancient bulge.

5.4. Nonaxisymmetric Bar/Bulge Potential

Since most of our stars orbit close to the Galactic center ($R_{\rm peri} < 3.5$ kpc) we additionally studied their kinematics in a nonaxisymmetric bar/bulge potential (Section 4.2).

In Figure 10 we can see that, first of all, changing the potential modifies the total energy (E_n) that stars possess nowadays. Besides, in their motion in the Galactic nonaxisymmetric bar potential, both total energy and the angular momentum component along the z-axis evolve with time. Clearly, total energy and angular momentum along the z-axis are no longer conserved. The Jacobi integral $E_J = E_n - \Omega_b L_z$ is constant instead. As a result of the evolution of the bulge/bar with time, E_n anticorrelates with L_z in the same fashion (same slope) for all the stars (Tkachenko et al. 2023). For some stars, these changes are large and move them far from the location they had in the axisymmetric potential. This highlights the importance of bar/bulge structure in the dynamical evolution of these stars. However, it is worth mentioning that for the stars we identified as probable members of accretion events the change in position due to bar perturbations is not significant. The shifted points in the E_n–L_z diagram are still well inside the regions of the accretion events (GE, Thamnos 1, 2).

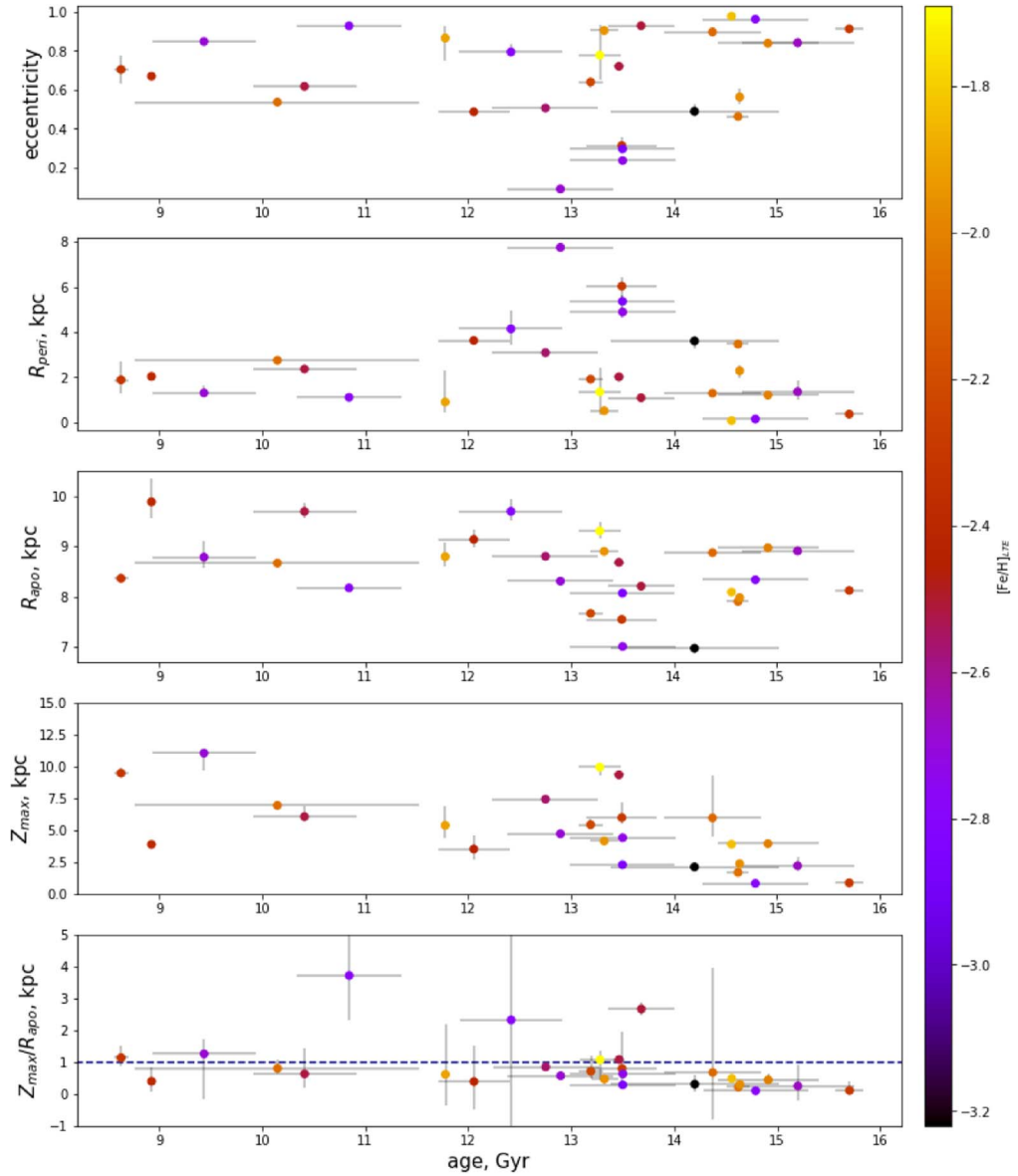

Figure 8. Correlation between eccentricity (e), pericenter ($R_{\rm peri}$), apocenter ($R_{\rm apo}$), maximum height above the Galactic plane ($Z_{\rm max}$), $Z_{\rm max}/R_{\rm apo}$, and age color-coded with metallicity.

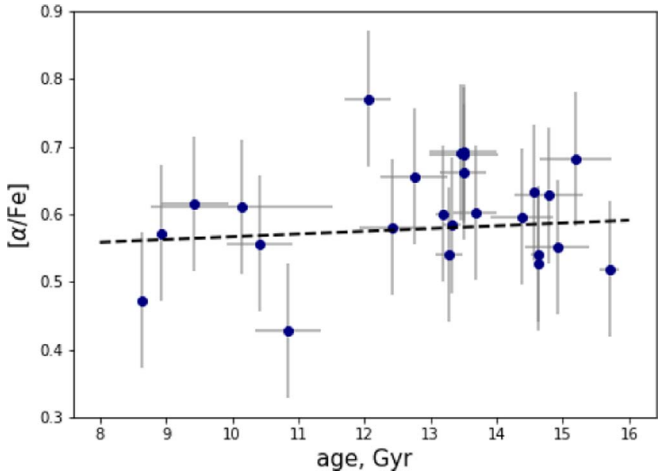

Figure 9. Correlation between α-elements and age. The dashed line shows the weighted fit.

For both potentials, we run simulations 1 Gyr long in time with step $\Delta t = 0.1$ Myr. For a nonaxisymmetric potential, though, we did not calculate uncertainties since it is a very time-consuming process.

6. Conclusions

Three main parameters that can be used to obtain the origin of the star are: kinematics, chemistry, and age. In this study, we explored all three of them for a sample of 28 very metal-poor stars for which we had previously derived ages (Plotnikova et al. 2022). Kinematics and chemistry are routinely used to assign stars to different components of the Milky Way galaxy, or to the various accreted systems that have been identified over the years in the Galactic halo. The basic conclusions of our study can be summarized as follows.

1. We have identified a group of stars with clear signatures of halo population according to their chemistry, age, and

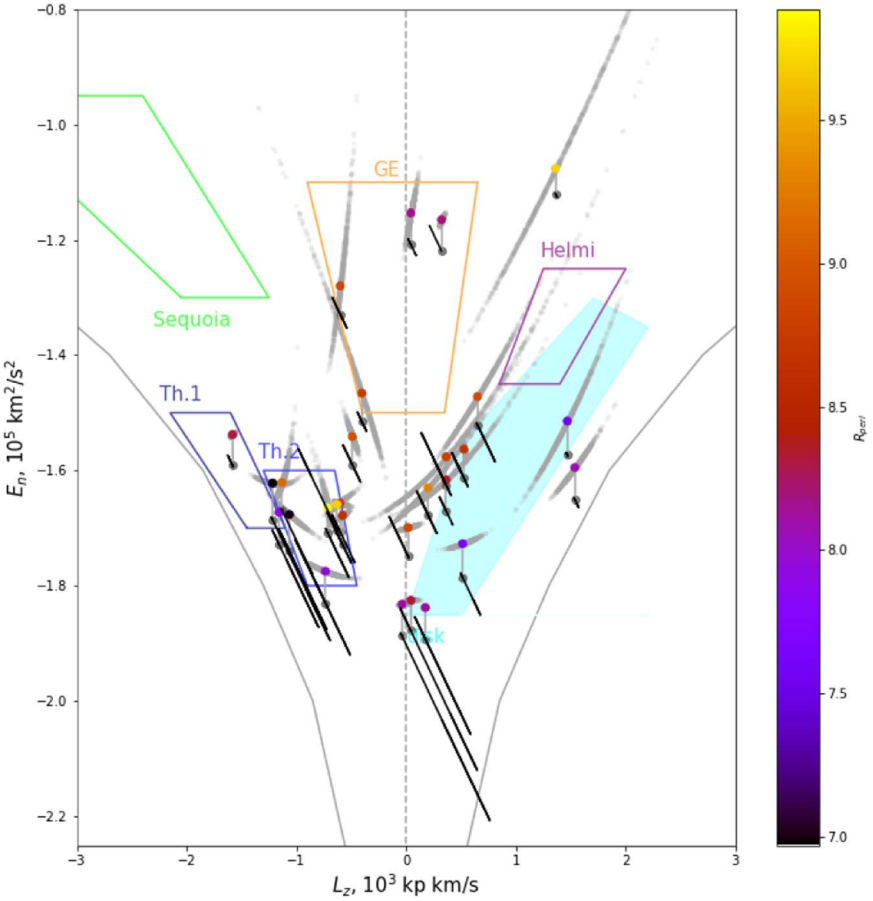

Figure 10. Comparison of the position in the E_n–L_z diagram calculated in axisymmetric (colored points with blue error bars) and nonaxisymmetric (black tilted lines) potentials. The E_n–L_z diagram includes the loci of the biggest known accretion events: Gaia–Enceladus/Sausage (GE, orange), Helmi stream (purple), Sequoia (green), Thamnos 1, 2 (dark blue, blue), and disk (cyan).

kinematics. However, we speculate that several of them, the oldest eight in fact, could have formed in the primordial bulge because of their orbital parameters (large eccentricity and low $Z_{\max}$ mostly) and large α-abundance.

2. We have identified another group of stars that we tentatively associate with Gaia–Enceladus/Sausage and Thamnos 1, 2 according to their similarity in kinematics, chemistry, and age.

The identification of a group, although small, of stars probably belonging to the infant bulge is rather intriguing. In fact, it supports a scenario in which the first component of the Milky Way to form was the bulge via a fast collapse *à la* ELS (Eggen et al. 1962). The other components then assembled with a major contribution from systems that were engulfed into the Milky Way later on, in agreement with the widely accepted merging scheme (Searle & Zinn 1978).

The comments of an anonymous referee have been much appreciated. A.P. acknowledges the Ulisse program of Padova University, which allowed her to spend a period at Concepcion University, where part of this work was done. Also, A.P. acknowledges Roman Tkachenko for the useful consultations. S.V. gratefully acknowledges the support provided by Fondecyt regular No. 1220264 and by the ANID BASAL projects ACE210002 and FB210003. S.O. acknowledges DOR 2020, University of Padova.

ORCID iDs

Anastasiia Plotnikova https://orcid.org/0000-0002-7504-0950
Giovanni Carraro https://orcid.org/0000-0002-0155-9434
Sandro Villanova https://orcid.org/0000-0001-6205-1493
Sergio Ortolani https://orcid.org/0000-0001-7939-5348

References

Astropy Collaboration, Price-Whelan, A. M., Lim, P. L., et al. 2022, ApJ, 935, 167
Astropy Collaboration, Price-Whelan, A. M., Sipőcz, B. M., et al. 2018, AJ, 156, 123
Astropy Collaboration, Robitaille, T. P., Tollerud, E. J., et al. 2013, A&A, 558, A33
Bailer-Jones, C. A. L., Rybizki, J., Fouesneau, M., Demleitner, M., & Andrae, R. 2021, AJ, 161, 147
Barklem, P. S., Christlieb, N., Beers, T. C., et al. 2005, A&A, 439, 129
Belokurov, V., Erkal, D., Evans, N. W., Koposov, S. E., & Deason, A. J. 2018, MNRAS, 478, 611
Bland-Hawthorn, J., & Gerhard, O. 2016, ARA&A, 54, 529
Bovy, J. 2015, ApJS, 216, 29
Bovy, J., Leung, H. W., Hunt, J. A. S., et al. 2019, MNRAS, 490, 4740
Bullock, J. S., & Johnston, K. V. 2005, ApJ, 635, 931
Carraro, G., Girardi, L., & Chiosi, C. 1999, MNRAS, 309, 430
Chemel, A. A., Glushkova, E. V., Dambis, A. K., et al. 2018, AstBu, 73, 162
Clarke, J. P., Wegg, C., Gerhard, O., et al. 2019, MNRAS, 489, 3519
Courteau, S., de Jong, R. S., & Broeils, A. H. 1996, ApJL, 457, L73
Drimmel, R., & Poggio, E. 2018, RNAAS, 2, 210
Eggen, O. J., Lynden-Bell, D., & Sandage, A. R. 1962, ApJ, 136, 748
François, P., Depagne, E., Hill, V., et al. 2007, A&A, 476, 935

Fulbright, J. P. 2000, AJ, 120, 1841
Gadotti, D. A., & dos Anjos, S. 2001, AJ, 122, 1298
Gaia Collaboration 2021, A&A, 649, A1
Gaia Collaboration, Vallenari, A., Brown, A. G. A., et al. 2022, arXiv:2208.00211
GRAVITY Collaboration, Abuter, R., Amorim, A., et al. 2018, A&A, 615, L15
Grenon, M. 1985, in Cool Stars with Excesses of Heavy Elements, ed. M. Jaschek & P. C. Keenan, Vol. 114 (Berlin: Springer), 147
Grillmair, C. J. 2017, ApJ, 847, 119
Helmi, A. 2002, Ap&SS, 281, 351
Helmi, A., Babusiaux, C., Koppelman, H. H., et al. 2018, Natur, 563, 85
Howes, L. M., Asplund, M., Keller, S. C., et al. 2016, MNRAS, 460, 884
Ibata, R. A., Lewis, G. F., Irwin, M. J., & Cambrésy, L. 2002, MNRAS, 332, 921
Johnson, C. I., Rich, R. M., Kobayashi, C., & Fulbright, J. P. 2012, ApJ, 749, 175
Johnson, C. I., Rich, R. M., Kobayashi, C., Kunder, A., & Koch, A. 2014, AJ, 148, 67
Koppelman, H. H., Helmi, A., Massari, D., Price-Whelan, A. M., & Starkenburg, T. K. 2019, A&A, 631, L9
Lindegren, L., Bastian, U., Biermann, M., et al. 2021, A&A, 649, A4
Lucey, M., Hawkins, K., Ness, M., et al. 2022, MNRAS, 509, 122
McMillan, P. J. 2017, MNRAS, 465, 76
Myeong, G. C., Vasiliev, E., Iorio, G., Evans, N. W., & Belokurov, V. 2019, MNRAS, 488, 1235
Nordlander, T., & Lind, K. 2017, A&A, 607, A75
Plotnikova, A., Carraro, G., Villanova, S., & Ortolani, S. 2022, ApJ, 940, 159
Portail, M., Gerhard, O., Wegg, C., & Ness, M. 2017, MNRAS, 465, 1621
Portail, M., Wegg, C., Gerhard, O., & Martinez-Valpuesta, I. 2015, MNRAS, 448, 713
Queiroz, A. B. A., Anders, F., Chiappini, C., et al. 2020, A&A, 638, A76
Reddy, B. E., Lambert, D. L., & Allende Prieto, C. 2006, MNRAS, 367, 1329
Reddy, B. E., Tomkin, J., Lambert, D. L., & Allende Prieto, C. 2003, MNRAS, 340, 304
Reid, M. J., & Brunthaler, A. 2004, ApJ, 616, 872
Roederer, I. U., Preston, G. W., Thompson, I. B., et al. 2014, AJ, 147, 136
Ruiz-Lara, T., Matsuno, T., Lövdal, S. S., et al. 2022, A&A, 665, A58
Sanders, J. L., Smith, L., Evans, N. W., & Lucas, P. 2019, MNRAS, 487, 5188
Searle, L., & Zinn, R. 1978, ApJ, 225, 357
Sestito, F., Venn, K. A., Arentsen, A., et al. 2023, MNRAS, 518, 4557
Simmerer, J. 2004, AAS Meeting, 205, 77.05
Sormani, M. C., Binney, J., & Magorrian, J. 2015, MNRAS, 454, 1818
Tkachenko, R., Korchagin, V., Jmailova, A., Carraro, G., & Jmailov, B. 2023, Galax, 11, 26
VandenBerg, D. A., Bond, H. E., Nelan, E. P., et al. 2014, ApJ, 792, 110
Wegg, C., & Gerhard, O. 2013, MNRAS, 435, 1874
Yeh, F.-C., Carraro, G., Korchagin, V. I., Pianta, C., & Ortolani, S. 2020, A&A, 635, A125
Yong, D., Norris, J. E., Bessell, M. S., et al. 2013, ApJ, 762, 26
Yuan, Z., Myeong, G. C., Beers, T. C., et al. 2020, ApJ, 891, 39